CrossMark

RESEARCH ARTICLE

An exact Hamiltonian coupled-mode system with application to extreme design waves over variable bathymetry

G. A. Athanassoulis[1,2] · K. A. Belibassakis[1] · Ch. E. Papoutsellis[1]

Abstract A novel, exact, Hamiltonian system of two non-linear evolution equations, coupled with a time-independent system of horizontal differential equations providing the Dirichlet-to-Neumann operator for any bathymetry, is applied to the study of the evolution of wave trains in finite depth, aiming at the identification of nonlinear high waves in finite depth, and over a sloping bottom. The vertical structure of the wave field is exactly represented up to the instantaneous free surface, by means of an appropriately constructed, rapidly convergent, local vertical series expansion of the wave potential. This Hamiltonian system is used for studying the fully nonlinear refocusing of transient wave groups, obtained by linear backpropagation of high-amplitude wave trains constructed by the theory of quasi-determinism. The results presented give a first quantification of the effects of sloping bottom and of spectral bandwidth on rogue-wave dynamics and kinematics, in finite depth.

Keywords Rogue waves · Nonlinear water waves · Hamiltonian coupled-mode system · Finite depth · Variable bathymetry · Quasi-determinism theory

✉ Ch. E. Papoutsellis
cpapoutse@central.ntua.gr; cpapoutsellis@gmail.com

G. A. Athanassoulis
mathan@central.ntua.gr; makathan@gmail.com

K. A. Belibassakis
kbel@fluid.mech.ntua.gr

[1] National Technical University of Athens, School of Naval Architecture and Marine Engineering, Athens, Greece

[2] Research Center for High Performance Computing, ITMO University, St. Petersburg, Russia

1 Introduction

Extremely high ocean waves, also called abnormal, freak or rogue waves, are known to appear without previous warning and have detrimental impact on ships or structures that may encounter. Because of their great practical significant, and their amazing scientific interest, rogue waves have been intensively studied in the last 15 years (Olagnon and Athanassoulis 2001; Olagnon and Prevosto 2004, 2008; Dysthe et al. 2008; Kharif et al. 2009; Osborne 2010).

Various mechanisms have been proposed for the physical generation of rogue waves. Among them we mention, (1) the spatial focusing, due to currents or the bathymetry, (2) linear, dispersive focusing (Lindgren 1972; Boccotti 2000, 1983; Phillips et al. 1992; Adcock and Taylor 2014), and (3) nonlinear, self-focusing, as initiated by the discovery of the modulational instability (Benjamin and Feir 1967; Zakharov and Ostrovsky 2009) and exploited further using the non linear Schrödinger (NLS) equation for water waves, introduced and solved by Zakharov (1968) and Zakharov and Shabat (1972), and developed further by Trulsen and Dysthe (1996), Trulsen et al. (2000) and Grimshaw and Annenkov (2011) and many other authors; see also Shemer et al. (2010). Extensive reviews of the above physical mechanisms, including data of marine observations as well as laboratory experiments, are presented in Kharif and Pelinofsky (2003) and Onorato et al. (2013).

Although a great deal of existing work concerning rogue waves has been based on the assumption of weak nonlinearity, in the last years the development of numerical methods able to efficiently simulate the long-time wave evolution in the context of fully nonlinear potential flow permitted the study of rogue waves in generic sea conditions. In this direction, Clamond et al. (2006) performed simulations of the long-time evolution of a two-dimensional, localized, long

wave packet using the integral equation method of Clamond and Grue (2001) and the higher order spectral (HOS) method of Dommermuth and Yue (1987) and West and Brueckner (1987), and compared their computations with those resulting from the classical NLS and extended Dysthe equations; see also Slunyaev and Shrira (2013), Adcock and Taylor (2016) and Fedele et al. (2016). In the latter paper, the authors propose an alternative mechanism for the generation of rogues waves, based on the constructive interference of elementary waves and weakly nonlinear effects. Other authors considered realistic wave fields resulting from ocean wave spectra, e.g., JONSWAP, and investigated the formation of large waves, indicating the importance of retaining the nonlinearity of the problem (Ducrozet et al. 2007; Katsardi and Swan 2011; Bateman et al. 2012; Viotti et al. 2013).

The majority of the above studies is restricted to infinite or constant-finite water depth. However, variable bathymetry can be an essential feature of the nonlinear wave propagation problem (Viotti and Dias 2014). In this case, the wave field is not spatially periodic, making the implementation of spectral methods quite involved, and the wave slope is expected to be high, invalidating the use of slope-asymptotic wave models. To investigate high waves over bathymetry in their full complexity, we shall apply the new, exact, Hamiltonian coupled-mode system (HCMS) introduced in Athanassoulis and Papoutsellis (2015), and derived in detail in Papoutsellis and Athanassoulis (2017). This system contains two nonlinear and nonlocal, Hamiltonian evolution equations, and is becoming closed by means of a new formulation of the Dirichlet-to-Neumann (DtN) operator, which is equally efficiently implemented in flat bottom and in arbitrarily varying bathymetry. The HCMS can be seen as a greatly improved, Hamiltonian reformulation of the nonlinear coupled-mode system presented earlier by Athanassoulis and Belibassakis (2007) and Belibassakis and Athanassoulis (2011). In this approach, a dimensional reduction of the problem is achieved by means of the exact representation of the velocity potential by a rapidly convergent series expansion in the vertical direction (Athanassoulis and Papoutsellis 2017). No simplifying assumptions are required concerning the steepness and/or the deformation of the free-surface elevation and the seabed; thus, this formulation accounts for fully non-linear, dispersive water waves. For numerical implementation, the only "simplification" that enters the equations is the truncation of the rapidly convergent series expansion of the wave potential.

The present Hamiltonian coupled-mode system is applied to the simulation of high waves, with initial data derived by specific spectra, in accordance with the quasi-determinism theory. To this aim, a linearly focused wave train is produced by exploiting the properties of normal processes near a local maximum (Lindgren 1970), applied to ocean waves by Boccotti (1983) and Boccotti (2000), under the name of quasi-determinism theory. This wave train is linearly back-

propagated in the space domain, producing a disintegrated, dispersed waveform, as also described by Katsardi and Swan (2011) and Bateman et al. (2012). The latter, dispersed wave train is considered as initial condition and is propagated forward by means of the fully nonlinear HCMS. Various simulations are considered over flat and sloping seabeds, and the wave kinematics and dynamics of the nonlinearly focusing event are comparatively presented, illustrating the effect of combined nonlinearity, shoaling and diffraction.

2 Governing equations and numerical method

We consider two-dimensional water waves in a Cartesian coordinate system Oxz, with $z = 0$ corresponding to the mean water level. The time-dependent fluid domain $D_h^\eta(t)$ is a non-uniform strip, delimited vertically by the seabed $z = -h(x)$, and the free surface $z = \eta(x, t)$ which are assumed to be smooth:

$$D_h^\eta(t) = \left\{ (x, z) \in \mathbb{R}^2 : x \in [x_1, x_2], -h(x) < z < \eta(x, t) \right\}.$$

Under the assumption of irrotational flow, the fluid velocity $V(x, z, t)$ is represented by means of a scalar wave potential $\Phi = \Phi(x, z, t)$, as $V = \nabla \Phi = (\partial_x \Phi, \partial_z \Phi)$, where $\partial_x = \partial/\partial_x$, $\partial_z = \partial/\partial_z$. In the absence of surface tension and applied surface pressure, and for a fixed, impermeable seabed, the wave motion is governed by the following set of equations

$$\partial_x^2 \Phi + \partial_z^2 \Phi = 0, \quad \text{in} \quad D_h^\eta(t), \tag{1a}$$

$$\partial_x h \partial_x \Phi + \partial_z \Phi = 0, \quad z = -h(x), \tag{1b}$$

$$\partial_t \eta + \partial_x \eta \partial_x \Phi - \partial_z \Phi = 0, \quad z = \eta(x, t), \tag{1c}$$

$$\partial_t \Phi + \frac{1}{2} (\nabla \Phi)^2 + g\eta = 0, \quad z = \eta(x, t) \tag{1d}$$

where g is the acceleration of gravity. The main difficulty in the numerical implementation of the above formulation is that both the wave potential Φ and its domain of definition $D_h^\eta(t)$ are unknowns evolving in time. This problem is efficiently treated in the present paper, by the HCMS introduced by Athanassoulis and Papoutsellis (2015) and derived in detail in Papoutsellis and Athanassoulis (2017). A derivation of the HCMS is briefly described herein. The starting point is the well-known Luke's variational principle (Luke 1967): the fields $\eta(x, t)$ and $\Phi(x, z, t)$ satisfy Eq. (1) if and only if they satisfy the variational equation

$$\delta \mathbb{S}[\eta, \Phi; \delta\Phi, \delta\eta] = \delta_\Phi \mathbb{S}[\eta, \Phi; \delta\Phi] + \delta_\eta \mathbb{S}[\eta, \Phi; \delta\eta] = 0, \tag{2a}$$

with action functional

$$\mathcal{S}[\eta, \Phi] = \int_{t_1}^{t_2} \int_{x_1}^{x_2} \int_{-h}^{\eta} \left(\partial_t \Phi + \frac{1}{2} |\nabla \Phi|^2 + gz \right) dz dx dt. \tag{2b}$$

In Eq. (2a), $\delta_\Phi \mathcal{S}[\eta, \Phi; \delta\Phi]$ and $\delta_\eta \mathcal{S}[\eta, \Phi; \delta\eta]$ denote the first partial variations (functional derivatives) of $\mathcal{S}[\eta, \Phi]$ with respect to Φ and η, in the directions $\delta\Phi$ and $\delta\eta$, respectively. Following Athanassoulis and Belibassakis (2000) and Belibassakis and Athanassoulis (2011), the wave potential Φ in the functional (2b) is exactly represented by a series expansion of the form

$$\Phi(x, z, t) = \sum_{n=-2}^{\infty} \varphi_n(x, t) Z_n(z; h(x), \eta(x, t)) \tag{3}$$

where $Z_n(z; h(x), \eta(x, t))$, $n \geq -2$, are known vertical basis functions depending on $h(x)$, $\eta(x, t)$ and the numerical parameters h_0 and μ_0 (see Appendix), and $\varphi_n(x, t)$ are unknown modal amplitudes. As proved in detail in Athanassoulis and Papoutsellis (2017), the series appearing in Eq. (3), together with its first- and second-order term-wise derivatives, converge throughout $D_h^\eta(t)$, up to and including the boundaries, provided the latter are smooth. Invoking the governing variational equation (2a), in conjunction with Eq. (3), a nonlinear coupled-mode system of evolution equations for $(\eta(x, t), \varphi_n(x, t))$ is derived. These equations contain infinite series summed over all modal amplitudes $\varphi_n(x, t)$. As shown by Papoutsellis and Athanassoulis (2017), exploiting the convergence properties of the series expansion (3), and introducing the free-surface potential $\psi := \Phi(x, \eta(x, t), t) = \sum_{n=-2}^{\infty} \varphi_n[Z_n]_{z=\eta}$, the aforementioned system can be transformed to a Hamiltonian system of two evolution equations for η and ψ, of the form

$$\partial_t \eta = -(\partial_x \eta)(\partial_x \psi) + \left((\partial_x \eta)^2 + 1 \right) \times \left(h_0^{-1} \mathcal{F}_{-2}[\eta, h]\psi + \mu_0 \psi \right), \tag{4a}$$

$$\partial_t \psi = -g\eta - \frac{1}{2}(\partial_x \psi)^2 + \frac{1}{2} \left((\partial_x \eta)^2 + 1 \right) \times \left(h_0^{-1} \mathcal{F}_{-2}[\eta, h]\psi + \mu_0 \psi \right)^2, \tag{4b}$$

where $\mathcal{F}_{-2}[\eta, h]\psi := \varphi_{-2}$ is determined, at every time t, by the solution of the coupled-mode system

$$\sum_{n=-2}^{\infty} \left(A_{mn}(\eta, h)\partial_x^2 + B_{mn}(\eta, h)\partial_x C_{mn}(\eta, h) \right) \varphi_n = 0,$$
$$m \geq -2, \tag{5a}$$

$$\sum_{n=-2}^{\infty} \varphi_n = \psi. \tag{5b}$$

Equations (4) and (5), along with appropriate lateral boundary conditions, constitute the Hamiltonian coupled-mode system (HCMS), already introduced as a term previously. In Eq. (5a), the variable coefficients are given by

$$A_{mn} = \int_{-h}^{\eta} Z_n Z_m dz, \tag{6a}$$

$$B_{mn} = 2 \int_{-h}^{\eta} (\partial_x Z_n) Z_m dz + (\partial_x h)[Z_m Z_n]_{z=-h}, \tag{6b}$$

$$C_{mn} = \int_{-h}^{\eta} (\partial_x^2 Z_n + \partial_z^2 Z_n) Z_m dz + \begin{pmatrix} \partial_x h \\ 1 \end{pmatrix} \times \left[(\partial_x Z_n, \partial_z Z_n) Z_m \right]_{z=-h}. \tag{6c}$$

The analytical calculation of the right-hand sides of Eq. (6) in terms of (η, h) is essential for the efficient numerical solution of the coupled-mode system, Eq. (5). Detailed derivation of the resulting expressions can be found in Papoutsellis et al. (2017). It should be noted that the introduction of ψ and the operator $\mathcal{F}_{-2}[\eta, h]$ in the evolutions equations (4), resembles, and in fact is inspired from, the introduction of the DtN operator $G[\eta, h]$ in the original Hamiltonian formulation of Eq. (1) (Zakharov 1968; Craig and Sulem 1993). We recall here that the standard DtN operator is defined by the expression $G[\eta, h]\psi = -\partial_x \eta[\partial_x \Phi]_{z=\eta} + [\partial_z \Phi]_{z=\eta}$, where Φ is determined by the solution of the boundary value problem consisting of Eq. (1a) in the instantaneous fluid domain $D_h^\eta(t)$, with the Neumann condition, Eq. (1c), on the fixed bottom, and the Dirichlet condition $\Phi(x, \eta(x, t), t) = \psi$ on the free surface. On the other hand, $\mathcal{F}_{-2}[\eta, h]\psi$ is determined by the solution of the linear coupled-mode system of differential equations (5) in the fixed horizontal domain $[x_1, x_2]$. The relation between $G[\eta, h]\psi$ and $\mathcal{F}_{-2}[\eta, h]\psi$ is recovered by taking into account the exact expansion of Φ, Eq. (3), with Z_n given by Eqs. (A1)–(A3). As shown by Athanassoulis and Papoutsellis (2017), the following equation holds true:

$$G[\eta, h]\psi = -(\partial_x \eta)(\partial_x \psi) + \left((\partial_x \eta)^2 + 1 \right) \times \left(h_0^{-1} \mathcal{F}_{-2}[\eta, h]\psi + \mu_0 \psi \right).$$

The solution of Eq. (5), say $\mathcal{F}_n[\eta, h]\psi := \varphi_n(x, t), n \geq -2$, actually gives us access to the entire instantaneous velocity potential $\Phi(x, z, t)$, by virtue of Eq. (3). Consequently, all physically interesting fluid quantities (e.g., velocity and pressure fields in the evolving fluid domain) can be accurately and efficiently computed, along the free-surface wave evolution.

To implement the Hamiltonian CMS Eqs. (4–6), the time-independent system Eq. (5) is truncated at a finite order N_{tot} corresponding to the modes kept in the expansion (3). The truncated system is solved by using fourth-order finite differences on a uniform grid of spacing δx. This procedures establishes an approximation of $\mathcal{F}_{-2}[\eta, h]\psi$ in terms of η, h and ψ. Numerical investigation in flat bottom, horizontally

periodic, test cases, where exact expressions of $\mathcal{F}_{-2}[\eta, h]\psi$ are available, revealed that this approximation, denoted by $\mathcal{F}_{-2}^{(N_{tot})}[\eta, h]\psi$, converges very rapidly to its exact value: the relative L^2-error decays as $O(N_{N_{tot}}^{-6.5})$, independently of the deformation of η; see Athanassoulis and Papoutsellis (2017). This feature is of great importance in unsteady wave simulations involving abrupt and large deformations of the free surface. Having established an accurate procedure for the computation of $\mathcal{F}_{-2}^{(N_{tot})}[\eta, h]\psi$, the evolution equations (4) are marched in time by using the classical Runge–Kutta method, in its four-step, explicit version. This scheme has been so far validated in many physically demanding phenomena where strong nonlinearity, dispersion and bathymetry effects are present. These include, for example, harmonic generation due to submerged obstacles (Papoutsellis and Athanassoulis 2017) and solitary wave interactions with bathymetry and vertical walls (Papoutsellis et al. 2017). In this paper, we shall examine the ability of this formulation to simulate the occurrence of waves of large amplitude, localized in space and time, through the nonlinear evolution of a dispersed wave train of low amplitude. One of the main difficulties in implementing such an application is the construction of the initial wave field $(\eta_0, \psi_0) = (\eta(x, 0), \psi(x, 0))$. This is done in the context of the theory of quasi-determinism, as described in the next section.

3 Simulation of high waves by nonlinear focusing of transient wavegroups

3.1 Initial conditions leading to a focusing event

To apply the nonlinear Hamiltonian CMS to the simulation of high waves, we need appropriately designed initial data, able to give rise to nonlinear focusing. Such kind of data will be derived from linearly focused wavegroups, belonging to specific sea states, as proposed by Katsardi and Swan (2011) and Bateman et al. (2012). The theoretical background permitting us to identify the spatial structure of such wavegroups is the Slepian theory of stationary Gaussian stochastic surfaces (Lindgren 1970, 1972), applied to the ocean waves under the name of *quasi-determinism theory* by Boccotti (1983, 2000). A quick, hopefully clear, description of the construction of the initial data compatible with a given sea state and leading to a focusing wave event, is given below.

Consider a specific sea state, described by means of a wave spectrum, either in the frequency or in the wavenumber formulation, $S(\omega)$ or $S(k)$ ($S(\omega)d\omega = S(k)dk$). The space–time representation of the free-surface elevation and the free-surface potential of such a sea state, with spectrum $S(k)$ spanning the wavenumber range (k_{min}, k_{max}), are given by the equations

$$\eta(x, t) = \sum_{n=1}^{N} a_n \cos(k_n x - \omega_n t + \varepsilon_n), \tag{7a}$$

$$\psi(x, t) = \sum_{n=1}^{N} \frac{g a_n}{\omega_n} \sin(k_n x - \omega_n t + \varepsilon_n), \tag{7b}$$

where $\{k_n\} = \{k_n, n = 1, 2, \ldots, N\}$ is a discrete set of wavenumbers spanning the support (k_{min}, k_{max}) of $S(k)$, $\{\omega_n\}$ is the corresponding set of angular frequencies, ε_n are random phases, uniformly distributed in $[-\pi, \pi]$, and the amplitudes a_n are expressed in terms of the spectral density $S(k)$ (see Eq. (4), below). Any concrete choice of random phases $\{\varepsilon_n\} = \{\varepsilon_n, n = 1, 2, \ldots, N\}$ corresponds to a specific realization of a wave system, compatible with (belonging to) the given spectrum. The identification of random phases corresponding to a linearly focused wave profile will be now accomplished by invoking the theory of quasi-determinism.

According to the quasi-determinism theory (Boccotti 2000), spectrum-compatible wave profiles with high maximum amplitude A, occurring at $x = 0, t = 0$, have the form

$$\eta_{foc}(x) \approx A \frac{R_{\eta\eta}(x)}{R_{\eta\eta}(0)}, \tag{8}$$

where $R_{\eta\eta}(x) = \langle \eta(0, 0)\eta(x, 0) \rangle$ is the spatial autocorrelation function of the free-surface elevation. Recalling the Wiener–Khinchin theorem,

$$R_{\eta\eta}(x) = \int_0^\infty S(k) \cos(kx) dk,$$

$$S(k) = \frac{2}{\pi} \int_0^\infty R_{\eta\eta}(x) \cos(kx) dx,$$

we can rewrite Eq. (8) in the form

$$\eta_{foc}(x) \approx A \frac{R_{\eta\eta}(x)}{R_{\eta\eta}(0)} = A \frac{\int_{k_{min}}^{k_{max}} S(k) \cos(kx) dk}{\int_{k_{min}}^{k_{max}} S(k) dk}. \tag{9}$$

Discretizing the integral in the numerator of the right-hand side of the above equation, we obtain

$$\eta_{foc}(x) \approx A \frac{\sum_{n=1}^{N} \cos(k_n x) \int_{k_n}^{k_{n+1}} S(k) dk}{\int_{k_{min}}^{k_{max}} S(k) dk}$$

$$= \sum_{n=1}^{N} a_n \cos(k_n x), \tag{10}$$

where

$$a_n = A \frac{\int_{k_n}^{k_{n+1}} S(k) dk}{\int_{k_{min}}^{k_{max}} S(k) dk}. \tag{11}$$

To the free-surface elevation field $\eta_{\text{foc}}(x)$ is associated, in the context of the linear wave theory, the free-surface potential

$$\psi_{\text{foc}}(x) = \sum_{n=1}^{N} \frac{g a_n}{\omega_n} \sin(k_n x). \tag{12}$$

Comparing Eqs. (10) and (12), with Eqs. (7a, 7b), we see that the high-amplitude (linearly focused at $x = 0$, $t = 0$) wave train $(\eta_{\text{foc}}(x), \psi_{\text{foc}}(x))$ occurs as a superposition of in-phase harmonics. However improbable this wave train may be, it represents a dangerous wave scenario, compatible with a given spectrum describing a realistic sea state. Such a wave system propagates, under linear dynamics, in accordance with Eqs. (1a, 1b), with $\varepsilon_n = 0$, and disintegrates, as time evolves, to a dispersive wave train of significantly lower amplitude(s). Such a disintegrated, thus fairly linear, version of $(\eta_{\text{foc}}(x), \psi_{\text{foc}}(x))$ will be taken as the initial data for starting a nonlinear wave propagation. This is done as described below.

The linearly focused wave, constructed above, is linearly back-propagated by a negative time shifting t_*, providing the fields

$$\eta_*(x, t = -t_*) = \sum_{n=1}^{N} a_n \cos(k_n x - \omega_n(-t_*)), \tag{13a}$$

$$\psi_*(x, t = -t_*) = \sum_{n=1}^{N} \frac{g a_n}{\omega_n} \sin(k_n x - \omega_n(-t_*)). \tag{13b}$$

These fields, which are of small steepness when t_* is sufficiently long (several peak periods), are used to define the initial conditions for the nonlinear wave propagation,

$$\eta_0(x) = \eta_*(x, t = -t_*), \quad \psi_0(x) = -\psi_*(x, t = -t_*), \tag{14}$$

aiming at a realistic modelling of the focusing process, taking into account the nonlinearity. The minus sign in the initial values of the free-surface potential is needed in order to transform the back-propagating system (η_*, ψ_*) to a forward-propagating one.

The above procedure for deriving the initial wavegroup is applied, in Sect. 4, both to the flat bottom and the depth-transition cases. Its validity for the second case is ensured from the fact that the initial wavegroup is essentially supported in the flat bottom region; see Fig. 5. That is, in all cases, we study how a deep-water wave group evolves, under fully nonlinear dynamics, either over a flat bottom or over a shoaling."

3.2 The TMA spectrum

To make concrete, realistic choices of the initial fields $\eta_0(x)$, $\psi_0(x)$, by means of Eq. (14), we need to specify the ampli-

tudes a_n, appearing in Eq. (13). For this purpose, a spectrum $S(k)$ and a value for the maximum amplitude A should be selected. To be consistent with finite-depth effects, the TMA spectrum is considered. This spectrum is introduced by Kitaigordskii et al. (1975), on the basis of dimensional arguments, as a modification of Phillips' spectrum, and is developed in its standard form, as a modification of the JON-SWAP spectrum, by Hughes, Vincent, Bouws and others; see, e.g., Hughes (1984), Bouws et al. (1985), Massel (1989, Ch. 7), and Recommended Practice (DNV-RP-C205 2010). The TMA spectrum is given by

$$S(\omega, h) \equiv S_{\text{TMA}}(\omega, h) = S_{\text{JS}}(\omega) r(\omega_h), \tag{15}$$

where $S_{\text{JS}}(\omega)$ is the JONSWAP spectrum, and $r(\omega_h)$, with $\omega_h = \omega\sqrt{h/g}$, is a depth- and frequency-dependent function, introduced to transform the ω^{-5} deep-water tail form to its finite-depth water equivalent. The JONSWAP spectrum is given by

$$S_{\text{JS}}(\omega) = \alpha(\gamma) S_{\text{PM}}(\omega) \gamma^{\delta(\omega)}, \tag{16}$$

where $S_{\text{PM}}(\omega)$ is the Pierson–Moskowitz spectrum,

$$S_{\text{PM}}(\omega) = \frac{5}{16} H_{\text{s}}^2 \omega_p \left(\frac{\omega}{\omega_p}\right)^{-5} \exp\left(-\frac{5}{4}\left(\frac{\omega}{\omega_p}\right)^{-4}\right), \tag{17}$$

(H_{s} is the significant wave height, $\omega_{\text{p}} = 2\pi/T_{\text{p}}$ is the angular spectral peak frequency), γ is a non-dimensional peak-shape parameter, ranging from 1 to 7, with default value $\gamma = 3.3$,

$$\delta(\omega) = \exp\left(-\frac{1}{2}\left(\frac{\omega - \omega_{\text{p}}}{\sigma \omega_{\text{p}}}\right)^2\right),$$

$$\sigma = \begin{cases} \sigma_a = 0.07, & \text{for } \omega \leq \omega_{\text{p}}, \\ \sigma_b = 0.09, & \text{for } \omega > \omega_{\text{p}}, \end{cases} \tag{18}$$
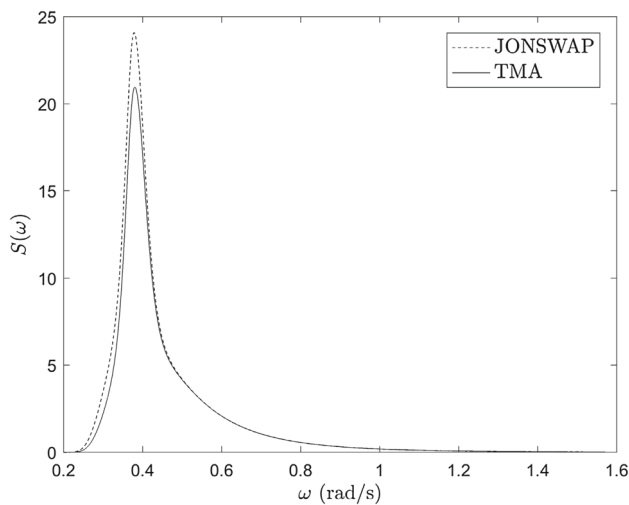
and $\alpha(\gamma) = 1 - 0.287\ln(\gamma)$ is a normalizing factor. For $\gamma = 1$, $S_{\text{JS}}(\omega) = S_{\text{PM}}(\omega)$. The function $r(\omega_h)$ is given by

$$r(\omega_h) = \frac{1}{F^2(\omega_h)}\left(1 + \frac{2\omega_h^2 F(\omega_*)}{\sinh\left(2\omega_h^2 F(\omega_h)\right)}\right)^{-1}, \quad \text{with}$$

$$F(\omega_h) = \tanh^{-1}(k_h)$$

where $k_h = k_h(\omega_h)$ is obtained from the dispersion relation $\omega_h^2 = k_h \tanh(k_h)$; see, also Massel (1989, Ch.7). Once the frequency spectrum $S(\omega)$ is specified, the wavenumber spectrum $S(k)$ is obtained by

$$S(k) = S(\omega)\frac{\mathrm{d}\omega}{\mathrm{d}k} = S(\omega)\frac{1}{2}\frac{\omega}{k}\left(1 + \frac{2kh}{\sinh(2kh)}\right)$$

Fig. 1 TMA spectrum used in the simulations (*solid line*), for $h = 150$ m, $H_s = 6.47$ m, $T_p = 16.6$ s, and base JONSWAP form (*dashed line*)

and the methodology described previously can be applied in order to obtain the initial conditions Eq. (14).

4 Numerical results

In this section, the TMA spectrum is considered with $H_s = 6.47$ m and $T_p = 16.6$ s (see Fig. 1) in conjunction with a maximum crest elevation at the focusing point $A = 12.0$ m.

4.1 Investigation over flat bottom

To implement the method described in the previous section, a dense discrete set of frequencies is specified around the peak frequency $\omega_p = 2\pi/T_p = 0.3785$ s^{-1}, uniformly distributed in the interval $[\omega_{min}, \omega_{max}] = [0.2, 0.5\pi]$. The linearly focused wave is plotted in Fig. 2a. The initial wave field for the nonlinear simulation is obtained by a linear back-propagation time $t_* = -300$ s, corresponding to a starting time about 18 peak periods before the (linear) focusing point; see Fig. 2b. Nonlinear simulations are obtained by truncating the modal series Eq. (3) keeping a total of $N_{tot} = 11$ terms. This choice was made after a preliminary numerical investigation, ensuring numerical convergence and satisfactory conservation properties. More details concerning the convergence of the modal series Eq. (3) can be found in Athanassoulis and Papoutsellis (2017). The spatio-temporal discretization is $dx/\lambda_p = 1/300$ and $dt/T_p = 1/250$ respectively and the frequency parameter μ_0 is $\mu_0 = \omega_p^2/g$. A snapshot of the free-surface elevation at the instant which assumes its maximum value is shown in Fig. 2c, and as is there indicated this occurs 0.3 s earlier than the linear prediction $t = 0$. The maximum elevation is $\eta_{max} = 13.98$ m, that

is about 16.5% larger than the linear prediction $\eta_{max} = A = 12$ m, and the corresponding spatial profile is asymmetric. It should be noted that, in accordance with the computations of Slunyaev and Shrira (2013 Section 5), the instants of maximum free-surface elevation and maximum wave height ($H_{max} = 21.16$ m at $t = -0.93$ s) do not coincide. Nevertheless, we shall restrict our attention to the discrepancies observed between linear predictions and nonlinear simulations in the case of waves of maximum free-surface elevation. A characteristic difference is the asymmetry of the time history of the wave around the instant of focusing; see Fig. 3a. Note that we use an appropriate time shifting so that $t = 0$ always corresponds to the maximum crest elevation. The importance of nonlinear effects becomes even more evident when one considers the time series of free-surface horizontal velocity $[\partial_x \Phi]_{z=\eta}$; see Fig. 3b. Indeed, the maximum value of $[\partial_x \Phi]_{z=\eta}$ is 45% larger than the linear prediction. Similar trends are also reported in the higher order spectral computations of Bateman et al. (2012). Here, we shall also consider the effect of spectral bandwidth defined by $\nu = \sqrt{M_0 M_2/M_1^2 - 1}$ where M_n is the nth-order spectral moment. The case presented previously corresponds to $\nu = 0.3341$. The same simulation is performed for two more cases involving narrower bandwidths, namely $\nu = 0.2286$, and $\nu = 0.1040$, and the same energy. The corresponding time series of the free-surface elevation are compared in Fig. 4. It is observed that initial conditions with narrower bandwidths lead to larger maximum elevations. More precisely, for $\nu = 0.2286$ and $\nu = 0.1040$ we have computed $\eta_{max} = 14.52$ m and $\eta_{max} = 15.85$ m, respectively.

4.2 The effect of sloping seabed

To examine the implication of a sloping seabed to the focusing process under study, a linear depth transition is introduced, reducing the depth from $h = 150$ m (in the deeper water region) to $h = 50$ m (in the shallower water region) within an extent of 2 km (slope 5%). In the first example the depth variation starts at $x_{start} = -1$ km; see Fig. 5. The initial wave conditions correspond to the first example of the previous subsection. The evolution of maximum wave elevation in the time interval $[-300, 50]$ s, is compared with the case of flat seabed in Fig. 6. Two interesting facts can be observed in this figure. First, a rapid increase of the crest amplitude in the last 300 s of the evolution, from about 6 to 14 m. Second, the maximum surface elevation in the case of the flat domain (13.98 m attained at $x = 28.7$ m) is about 4% greater than the corresponding one for the case of the sloping seabed (13.46 m attained at $x = -182$ m). This fact has been also reported by other authors studying the phenomenon by CFD and experimentally; see, e.g., Cui et al. (2012). This behaviour can be attributed to combined diffrac-

Fig. 2 **a** Linearly focused event with $A = 12.0$ m. **b** Linearly back-propagated wave at $t_* = -300$ s. **c** Computed focusing event taking into account full nonlinearity
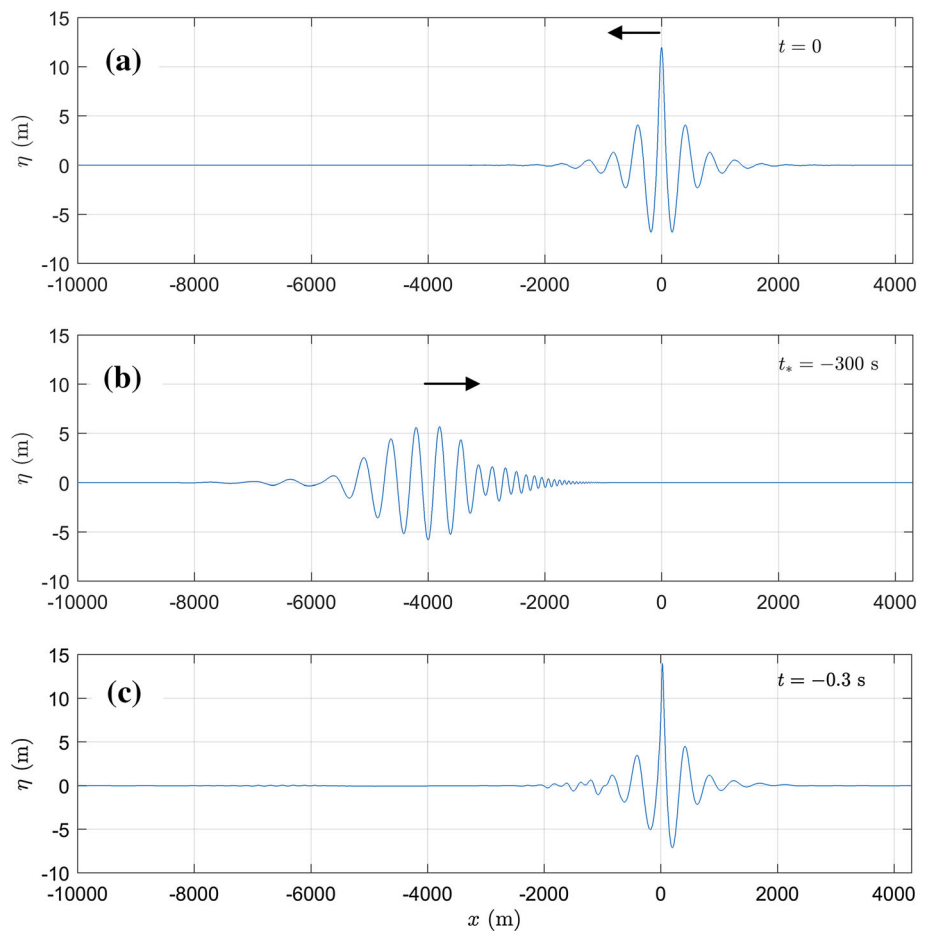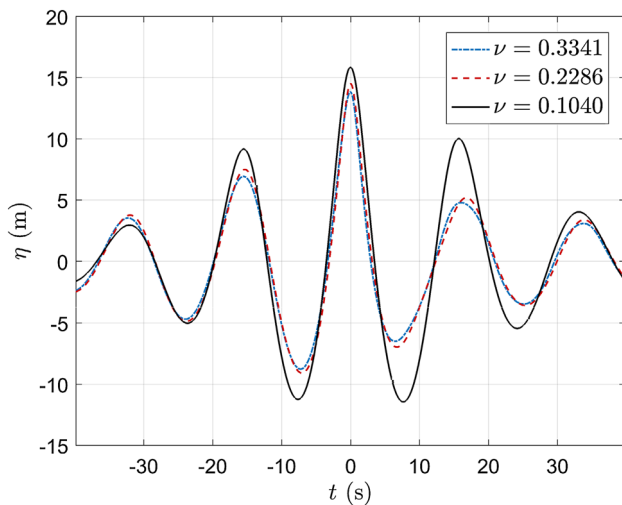

Fig. 3 Time series of the free-surface elevation and the free-surface horizontal velocity around the instant of the maximum elevation
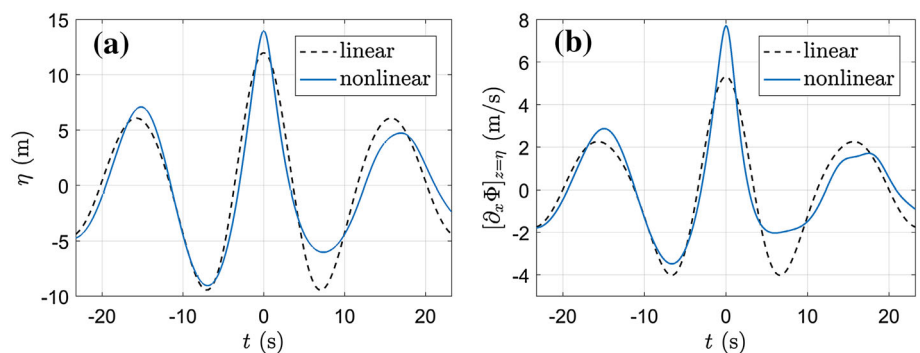

tion and shoaling effects, leading to the reflection of a small amount of energy of the incident wavegroup. In addition, the shortening of the wavelengths, due to shoaling, is associated with a small reduction of the propagation speed of the frequency components around the peak of the spectrum, which results in a more than one peak period delay of the focusing event in the case of the sloping seabed, in comparison with the flat bottom case. We remark that the conditions associated with the studied focused event correspond to quite nonlinear non-breaking waves. More precisely, at the location of the focused event we have $H_{max}/h = 0.14$ for the flat bottom case and $H_{max}/h = 0.2$ for the sloping seabed case.

For further comparison we have plotted, in Fig. 7, the free-surface elevation and horizontal velocity distribution for a time interval around the focusing instant. Clearly, this depth transition does not significantly affect the focusing of free-surface wave group. To further investigate the sensitivity of the focusing process to the starting point of the depth transition, we have also considered a starting point $x_{start} = -2$ km. The corresponding results are compared with the case $x_{start} = -1$ km in Fig. 8. The maximum surface elevation, in the case $x_{start} = -2$ km, is about one meter higher (14.43 m attained at $x = -27$ m) and occurs after a wave of

Fig. 4 Time series of the free-surface elevation around the instant of the maximum elevation for three different bandwidths
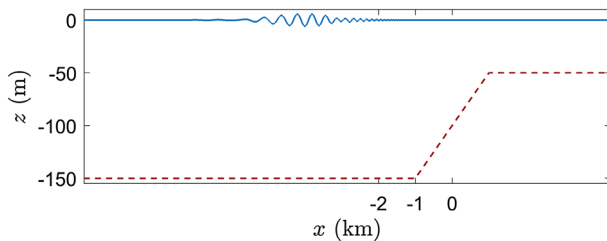
Fig. 5 Initial free surface and bathymetry for the sloping bottom case
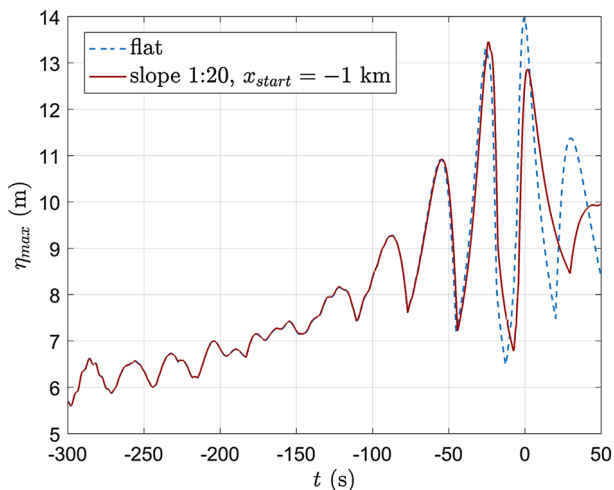
Fig. 6 Maximum wave elevation in the time interval $\Delta t = 350$ s during the nonlinear simulation for the flat bottom and sloping bottom case. According to linear theory, the large wave event occurs at $t = 0$ exhibiting maximum free-surface elevation $\eta_{max} = 12$ m

significantly large wave height (about 15 m), indicating that the interaction with the seabed is stronger.

Closing this section, we shall briefly comment on an important advantage of the present approach, that is the efficient calculation of the wave potential and related quantities in the entire fluid domain. This is a direct consequence of the specific local-mode representation Eq. (3), where the vertical functions Z_n are easily calculated using only information of the depth and the free-surface elevation. Exploiting this benefit, the distribution of the velocity potential and of the dynamic pressure at the focusing point are presented in the in Figs. 9 and 10, as predicted by the present nonlinear coupled-mode model, both in the horizontal flat domain and the sloping seabed 5%, respectively. We observe in these figures that for an extended region around the focusing point the value of the dynamic pressure remains high in the whole water column and attains significant values even at the seabed. This finding could be useful in the exploitation of bottom pressure measurements for the identification and study of such extreme events.
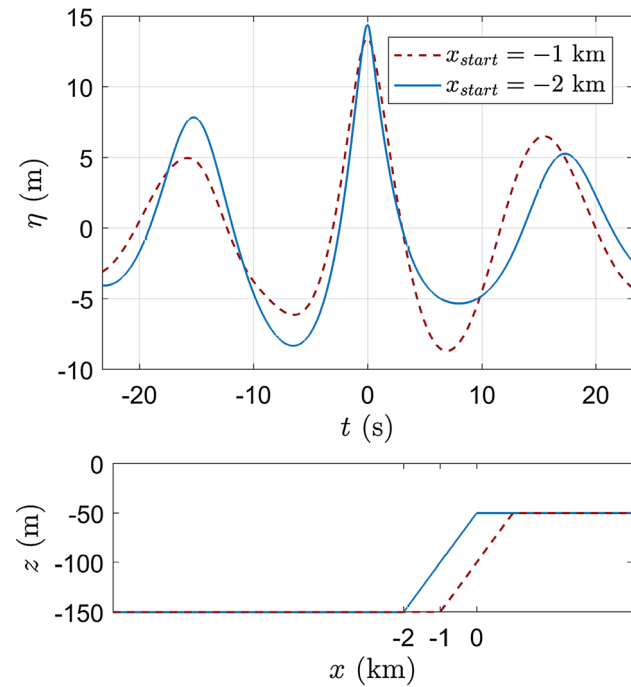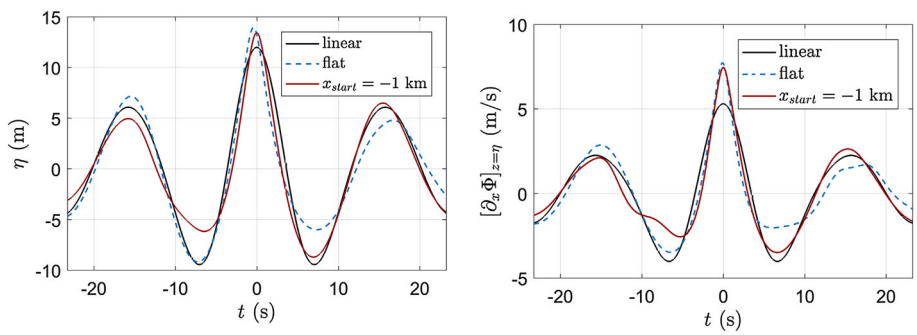
5 Conclusions

The Hamiltonian coupled-mode system (HCMS) of Athanassoulis and Papoutsellis (2015) (see also Papoutsellis and Athanassoulis 2017) has been applied to the simulation of the focusing of unidirectional transient wave groups that lead to large wave events over flat bottom and sloping seabed. No simplifying assumptions are made concerning the degree of retained nonlinearity and the vertical structure of the wave potential is exactly represented by an exact convergent series expansion.

The methodology adopted to obtain initial conditions for the nonlinear simulations is based on the theory developed by Lindgren (1972) and Boccotti (1983) (see also Bateman et al. (2012)) applied to the case of the TMA spectrum. Several simulations where performed illustrating the importance of retaining the full nonlinearity of the problem. In the flat bottom case, it is shown that (1) the nonlinear evolution leads to extreme waves with larger maximum elevations, in comparison with linear theory and (2) maximum elevation becomes larger as the bandwidth becomes narrower. In the sloping bottom case, we have considered two cases involving a linear shoaling of slope 5% staring at two different positions. This simple comparison showed that the wave–bottom interaction can be more significant when the starting point of the depth variation is well before the focusing point predicted by linear theory ($x = 0$). Moreover, the fluid kinematics dur-

Fig. 7 Free-surface elevation and horizontal velocity vs time around the instant of focusing: linear theory (*solid black line*), nonlinear computations, over flat seabed (*dashed blue line*) and over sloping seabed 5% (*solid red line*) (colour figure online)
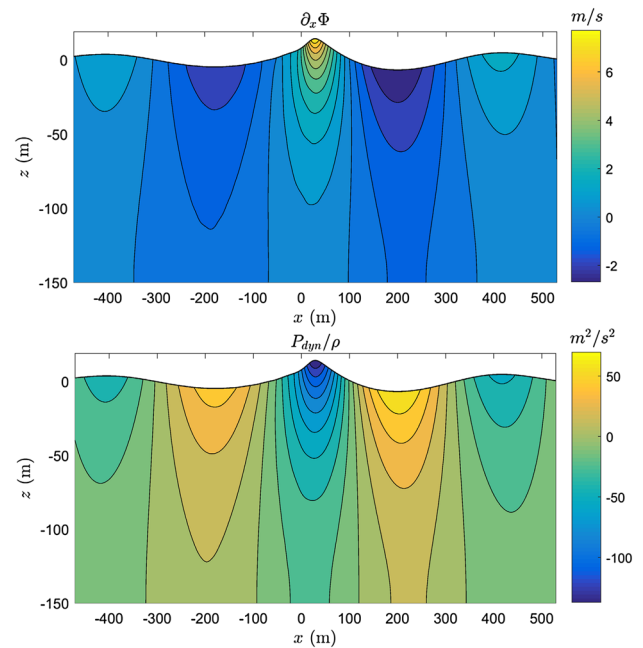

Fig. 8 Time series of the free-surface elevation on the formation of the focusing event

Fig. 9 Horizontal velocity and dynamic pressure of the extreme wave in the flat bottom case $h = 150$ m

ing the unsteady wave evolution can be easily and efficiently computed on the basis of the rapidly convergent series expansion of the wave potential. The present results show that the Hamiltonian coupled-mode system, being free of asymptotic assumptions and easy to implement numerically, provides a valuable tool for the study of rogue waves. More extensive investigation, including the effect of directionality and more complex three dimensional bottom topographies, will be studied in the future.

Appendix: Vertical basis functions

The vertical basis functions Z_n, $n \geq -2$, normalized so that $[Z_n]_{z=\eta} = 1$, $n \geq -2$, are given by

$$Z_{-2}(z; \eta, h) = \frac{\mu_0 h_0 + 1}{2h_0} \frac{(z+h)^2}{\eta + h}$$
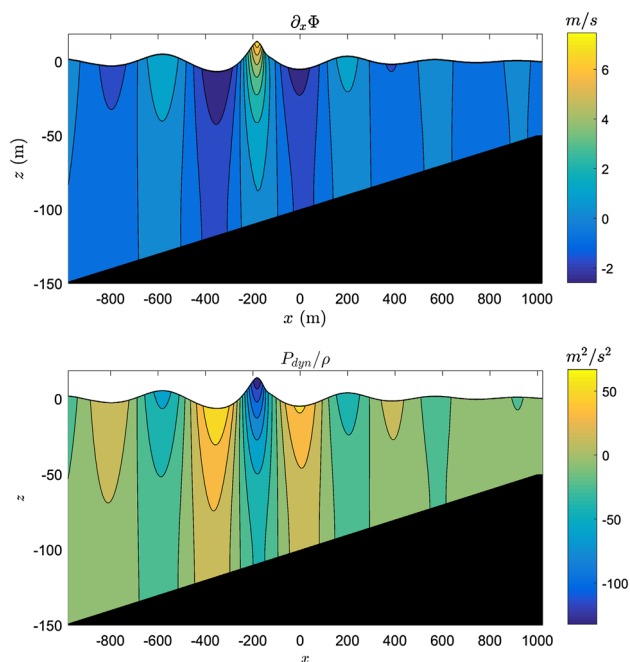
$$-\frac{\mu_0 h_0 + 1}{2h_0}(\eta + h) + 1, \tag{A1}$$

$$Z_{-1}(z; \eta, h) = \frac{\mu_0 h_0 - 1}{2h_0} \frac{(z+h)^2}{\eta + h} + \frac{1}{h_0}(z+h)$$

$$-\frac{\mu_0 h_0 + 1}{2h_0}(\eta + h) + 1 \tag{A2}$$

$$Z_0(z; \eta, h) = \frac{\cosh[k_0(z+h)]}{\cosh[k_0(\eta+h)]},$$

$$Z_n(z; h, \eta) = \frac{\cos[k_n(z+h)]}{\cos[k_n(\eta+h)]}. \tag{A3}$$

In the above definitions, the local functions $k_n = k_n(\boldsymbol{x}, t)$, $n \geq 0$ are functions implicitly given by the (local) transcendental equations

$$\mu_0 - k_0 \tanh[k_0(\eta + h)] = 0,$$

Fig. 10 Horizontal velocity and dynamic pressure of the extreme wave in the case of the sloping 5% seabed

$$\mu_0 + k_n \tan[k_n(\eta + h)] = 0, \qquad (A4)$$

where $\mu_0 > 0$ is an arbitrary constant, and h_0 (reference depth) is introduced for dimensional consistency.

References

Adcock T, Taylor P (2014) The physics of anomalous ("rogue") ocean waves. Rep Prog Phys 77:1–17. doi:10.1088/0034-4885/77/10/105901

Adcock T, Taylor P (2016) Fast and local non-linear evolution of steep wave-groups on deep water: a comparison of approximate models to fully non-linear simulations. Phys Fluids 28(1–2):16601. doi:10.1063/1.4938144

Athanassoulis G, Belibassakis K (2000) A complete modal expansion of the wave potential and its application to linear and nonlinear water-wave problems. In: Rogue waves. Brest, France, pp 73–90

Athanassoulis G, Belibassakis K (2007) New evolution equations for non-linear water waves in general bathymetry with application to steady travelling solutions in constant, but arbitrary depth. Discrete Contin Dyn Syst Supplement 2007 75–84

Athanassoulis G, Papoutsellis C (2015) New form of the Hamiltonian equations for the nonlinear water-wave problem, based on a new representation of the DtN operator, and some applications. In: Proceedings of the 34th international conference on ocean, offshore and Arctic Engineering. St. John's, Newfoundland, Canada: ASME, p V007T06A029. doi:10.1115/OMAE2015-41452

Athanassoulis G, Papoutsellis C (2017) Exact semi-separation of variables in waveguides with nonplanar boundaries. Proc R Soc Lond A 473:20170017. doi:10.1098/rspa.2017.0017

Bateman W, Katsardi V, Swan C (2012) Extreme ocean waves. Part I. The practical application of fully nonlinear wave modelling. Appl Ocean Res 34:209–224. doi:10.1016/j.apor.2011.05.002

Belibassakis KA, Athanassoulis GA (2011) A coupled-mode system with application to nonlinear water waves propagating in finite water depth and in variable bathymetry regions. Coast Eng 58(4):337–350. doi:10.1016/j.coastaleng.2010.11.007

Benjamin T, Feir J (1967) The disintegration of wave trains in deep water. J Fluid Mech 27(3):417–430. doi:10.1017/S002211206700045X

Boccotti P (1983) Some new results on statistical properties of wind waves. Appl Ocean Res 5(3):134–140

Boccotti P (2000) Wave mechanics for ocean engineering. Elsevier oceanography series, vol 64. Elsevier, Netherlands

Bouws E, Günther H, Rosenthal W, Vincent CL (1985) Similarity of the wind wave spectrum in finite depth water: 1. Spectral form. J Geophys Res Oceans 90(C1):975–986. doi:10.1029/JC090iC01p00975

Clamond D, Francius M, Grue J, Kharif C (2006) Long time interaction of envelope solitons and freak wave formations. Eur J Mech B/Fluids 25(5):536–553. doi:10.1016/j.euromechflu.2006.02.007

Clamond D, Grue J (2001) A fast method for fully nonlinear water-wave computations. J Fluid Mech 447:337–355. doi:10.1017/S0022112001006000

Craig W, Sulem C (1993) Numerical Simulation of Gravity Waves. J Comput Phys 108:73–83

Cui C, Zhang C, Yu X, Li B (2012) Numerical study on the effects of uneven bottom topography on freak waves. Ocean Eng 54:132–141. doi:10.1016/j.oceaneng.2012.06.021

DNV-RP-C205 (2010) Environmental conditions and environmental loads. https://rules.dnvgl.com/docs/pdf/dnv/codes/docs/2010-10/rp-c205.pdf

Dommermuth D, Yue D (1987) A high-order spectral method for the study of nonlinear gravity waves. J Fluid Mech 184:267–288. doi:10.1017/S002211208700288X

Ducrozet G, Bonnefoy F, Le Touzé D, Ferrant P (2007) 3-D HOS simulations of extreme waves in open seas. Nat Hazards Earth Syst Sci 7(1):109–122. doi:10.5194/nhess-7-109-2007

Dysthe K, Krogstad H, Muller P (2008) Oceanic rogue waves. Annu Rev Fluid Mech 40:287–310. doi:10.1146/annurev.fluid.40.111406.102203

Fedele F, Brennan J, Ponce de León S, Dudley J, Dias F (2016) Real world ocean rogue waves explained without the modulational instability. Sci Rep 6(1):27715. doi:10.1038/srep27715

Grimshaw R, Annenkov S (2011) Water wave packets over variable depth. Stud Appl Math 126:409–427

Hughes S (1984) The TMA shallow-water spectrum, description and applications. Tehnical Report CERC-84-7, Department of the Army, Waterways Experiment Station, Corps of Engineers. http://www.dtic.mil/dtic/tr/fulltext/u2/a157975.pdf

Katsardi V, Swan C (2011) The evolution of large non-breaking waves in intermediate and shallow water. I. Numerical calculations of unidirectional seas. Proc R Soc A Math Phys Eng Sci 467(2127):778–805. doi:10.1098/rspa.2010.0280

Kharif C, Pelinofsky E (2003) Physical mechanisms of the rogue wave phenomenon. Eur J Mech B Fluid 22(6):603–634

Kharif C, Pelinovsky E, Slunyaev A (2009) Rogue waves in the ocean. Springer, Berlin

Kitaigordskii S, Krasitskii V, Zaslavskii M (1975) On Phillips' theory of equilibrium range in the spectra of wind-generated gravity waves. J Phys Oceanogr 5:410–420

Lindgren G (1970) Some properties of a normal process near a local maximum. Ann Math Stat 41:1870–1883

Lindgren G (1972) Wave-length and amplitude in Gaussian noise. Adv Appl Probab 4:81–108

Luke JC (1967) A variational principle for a fluid with a free surface. J Fluid Mech 27:395–397

Massel S (1989) Hydrodynamics of coastal zones. Elsevier oceanography series, vol 48. Elsevier, Netherlands

Olagnon M, Athanassoulis G (eds) (2001) Rogue waves 2000. In: Rogue waves. IFREMER, Brest, France

Olagnon M, Prevosto M (eds) (2004) Rogue waves 2004. In: Rogue waves. IFREMER, Brest, France

Olagnon M, Prevosto M (eds) (2008) Rogue waves 2008. In: Rogue waves. IFREMER, Brest, France

Onorato M, Residori S, Bortolozzo U, Montina A, Arecchi T (2013) Rogue waves and their generating mechanisms in different physical contexts. Phys Rep 528(2):47–89. doi:10.1016/j.physrep.2013.03.001

Osborne A (2010) Nonlinear ocean waves and the inverse scattering transform. Elsevier, Amsterdam

Papoutsellis C, Athanassoulis G (2017) A new efficient Hamiltonian approach to the nonlinear water-wave problem over arbitrary bathymetry **(submitted)**. arXiv:1704.03276

Papoutsellis C, Athanassoulis G, Charalambopoulos A (2017) Interaction of solitary waves with varying bathymetry and vertical walls, using a fully nonlinear Hamiltonian coupled-mode theory **(in preparation)**

Phillips O, Gu D, Donelan M (1992) Expected structure of extreme waves in a Gaussian sea. Part I: Theory and SW ADE buoy measurements 0. J Phys Oceanogr 23:992–1000

Shemer L, Sergeeva A, Slunyaev A (2010) Applicability of envelope model equations for simulation of narrow-spectrum unidirectional random wave field evolution: experimental validation. Phys Fluids 22(1–9):16601. doi:10.1063/1.3290240

Slunyaev A, Shrira V (2013) On the highest non-breaking wave in a group: fully nonlinear water wave breathers versus weakly nonlinear theory. J Fluid Mech 735:203–248. doi:10.1017/jfm.2013.498

Trulsen K, Dysthe K (1996) A modified nonlinear Schrtidinger equation for broader bandwidth gravity waves on deep water. Wave Motion 24:281–289

Trulsen K, Kliakhandler I, Dysthe K, Velarde M (2000) On weakly nonlinear modulation of waves on deep water. Phys Fluids 12:2432–2437. doi:10.1063/1.1287856

Viotti C, Dias F (2014) Extreme waves induced by strong depth transitions: fully nonlinear results. Phys Fluids 26(5):51705, 1–7. doi:10.1063/1.4880659

Viotti C, Dutykh D, Dudley J, Dias F (2013) Emergence of coherent wave groups in deep-water random sea. Phys Rev E 87(1–2):63001. doi:10.1103/PhysRevE.87.063001

West J, Brueckner K (1987) A new numerical method for surface hydrodynamics. J Geophys Res 92(C11):11803–11824. doi:10.1029/JC092iC11p11803

Zakharov V (1968) Stability of periodic waves of finite amplitude on the surface of a deep fluid. J Appl Mech Tech Phys 9(2):86–94. doi:10.1007/BF00913182

Zakharov V, Ostrovsky L (2009) Modulation instability: the beginning. Physica D 238:540–548. doi:10.1016/j.physd.2008.12.002

Zakharov V, Shabat B (1972) Exact theory of two-dimensional self-focusing and one dimensional self-modulation of waves in nonlinear media. Sov Phys JETP 34:62–69